


## Chaos and bipartite entanglement between Bose-Josephson junctions

Amichay Vardi *Department of Chemistry, Ben-Gurion University of the Negev, Beer-Sheva 84105, Israel*

(Received 17 August 2022; accepted 2 December 2022; published 23 December 2022)

The entanglement between two weakly coupled bosonic Josephson junctions is studied in relation to the classical mixed phase space structure of the system, containing symmetry-related regular islands separated by chaos. The symmetry-resolved entanglement spectrum and bipartite entanglement entropy of the system's energy eigenstates are calculated and compared to their expected structure for random states that exhibit complete or partial ergodicity. The entanglement spectra of chaos-supported eigenstates match the microcanonical structure of a Generalized Gibbs Ensemble due to the existence of an adiabatic invariant that restricts ergodization on the energy shell. The symmetry-resolved entanglement entropy of these quasistochastic states consists of a mean-field maximum entanglement term and a fluctuation correction due to the finite size of the constituent subsystems. The total bipartite entanglement entropy of the eigenstates correlates with their chaoticity. Island-supported eigenstates are macroscopic Schrödinger cat states for particles and excitations with substantially lower entanglement.

DOI: [10.1103/PhysRevE.106.064210](https://doi.org/10.1103/PhysRevE.106.064210)

### I. INTRODUCTION

The study of quantum entanglement has lately focused on many-body systems, with important applications in quantum information and condensed matter physics [1,2]. Entanglement lies at the heart of quantum information processing [3] and quantum teleportation [4]. In condensed matter physics it underlies the density matrix renormalization group methodology [5–7], quantum phase transitions [8–10] and topological order [11], quantum quench dynamics [12–15], quantum thermalization [16–20], and many-body localization [21,22].

Considerable effort has recently been concentrated towards the study of bipartite entanglement in the stochastic-like eigenstates of quantum chaotic Hamiltonians [23–40]. The entanglement entropy of such states is near maximal, because chaotic ergodization implies the eigenvalues of the reduced subsystem density matrices are spread nearly uniformly, with a fluctuation correction due to the finite size of the subsystems [23,34].

So far, the analysis of eigenstate entanglement has focused on systems that exhibit “hard” chaos, i.e., their entire phase space is chaotic. However, in many-body systems with few classical degrees of freedom the phase space is often *mixed*, with “islands” of quasiintegrability due to the local conservation of residual motional constants, interspersed between chaotic “seas” in which the dynamics is ergodic. The ergodicity of such systems is incomplete and corresponds to *generalized Gibbs ensembles* (GGEs) rather than the canonical ensembles encountered in the presence of relaxation and pumping, or the microcanonical ensembles obtained for isolated systems. It is thus desirable to establish how bipartite quantum entanglement is affected by the partition of the classical phase space into regular and chaotic regions.

In this work, the  $U(1)$  symmetry resolved entanglement spectrum [2,11] and entanglement entropy [41–43] are studied

for the minimal model system of two weakly-coupled bosonic Josephson junctions. In a sense, this is the interacting many-body bosonic equivalent of the ubiquitous two qubits system in which the notion of bipartite entanglement first appears [44]. It was previously shown [45,46] that the timescale separation between the fast internal motion within each junction, and the slow exchange of particles and energy between them, implies the adiabatic invariance of the total number of Josephson excitations  $J$  corresponding in the classical limit to the sum of subsystem actions, in addition to the obvious conservation of the total system energy  $E$  and the number of particles  $N$ . The adiabatic system dynamics can thus be described as the slow motion of particles and Josephson quasiparticles (“josons”) between the constituent subsystems.

While for small perturbations around the stationary points, the classical dynamics of this system reduces to coupled Josephson oscillations [45–48]; at higher energy it is surprisingly rich. In particular, we find that the mutual conservation of  $E$  and  $J$  generates a mixed phase space structure, with integrable self-trapping islands of two types separated by a chaotic sea. The quantum eigenstates are correspondingly supported by the different classical phase-space regions. The bipartite entanglement entropies of the system's eigenstates are correlated with ergodicity measures such as the participation number and the Shannon entropy. The chaos-supported eigenstates exhibit the expected near maximal entanglement. By contrast, island-supported eigenstates are macroscopic Schrödinger cat states involving only  $\mathcal{O}(2)$  nonvanishing eigenvalues in the reduced subsystem density matrices. The population imbalance distribution and the symmetry resolved entanglement entropy of the chaotic eigenstates corresponds to a GGE that accounts for the adiabatic invariance of  $J$  within the respective energy shell.

The model system is introduced in Sec. II, its adiabatic dynamics is discussed in Sec. III, and the methodology for

evaluation the number of excitations is briefly recalled in Sec. IV. Subspace dimensionality notation is summarized in Sec. IV. The system's eigenstates and their relation to the mixed classical phase space are discussed in Sec. VI. The bipartition of the system and the symmetry-resolved entanglement spectrum are presented in Sec. VII. The expected particle imbalance and bipartite entanglement entropy distributions for ergodic and semiergodic states are compared in Sec. VIII with the numerically calculated distributions of the chaos-supported eigenstates, demonstrating the agreement with the GGE prediction. Recently employed experimental techniques for the measurement of symmetry resolved entanglement in bose-Hubbard systems are described in Sec. IX. Finally, summary and concluding remarks are provided in Sec. X.

## II. THE COUPLED DIMERS MODEL

Consider a system of two weakly-coupled bosonic Josephson junctions (AKA ‘‘Bose-Hubbard dimers’’), described by the four-mode Hamiltonian [45–48]

$$\hat{H} = -\frac{\Omega}{2} \left( \sum_{\alpha} \hat{a}_{+, \alpha}^{\dagger} \hat{a}_{-, \alpha} + H.c \right) + \frac{U}{2} \sum_{\alpha, \sigma} \hat{n}_{\sigma, \alpha} (\hat{n}_{\sigma, \alpha} - 1) - \frac{\omega}{2} \left( \sum_{\sigma} \hat{a}_{\sigma, L}^{\dagger} \hat{a}_{\sigma, R} + \hat{a}_{\sigma, R}^{\dagger} \hat{a}_{\sigma, L} \right), \quad (1)$$

where  $\hat{a}_{\sigma, \alpha}$  annihilate a boson in the  $\sigma = \pm$  mode of the  $\alpha = L, R$  junction. The interdimer coupling  $\omega$  is assumed to be much smaller than the coupling  $\Omega$  between the two modes of each dimer and the on-site interaction strength  $U$ . Below we rescale time as  $t \rightarrow \Omega t$  so that frequencies are given in units of  $\Omega$  and the dimensionless system parameters are  $w = \omega/\Omega \ll 1$  and  $u = UN/\Omega$ .

In the limit of large  $N$ , the restricted coherent-state (mean field) dynamics is obtained by replacing the operators  $\hat{a}_{\sigma, \alpha}$  with  $c$  numbers. The resulting classical motion has three degrees of freedom, e.g., three population imbalances and three relative phases between the classical amplitudes serving as action-angle variables.

## III. ADIABATIC DYNAMICS

The dynamics of the double-dimer model in the adiabatic limit  $w \ll 1$  was reduced by Strzys and Anglin [45,46], to the slow exchange of particles and ‘‘josons’’ between the two subsystems. Their procedure begins with a Holstein-Primakoff transformation (HPT) applied to Eq. (1):

$$\begin{aligned} \frac{n_{\alpha}}{2} - \hat{A}_{\alpha}^{\dagger} \hat{A}_{\alpha} &\equiv \frac{1}{2} (\hat{a}_{\alpha, +}^{\dagger} \hat{a}_{\alpha, -} + \hat{a}_{\alpha, -}^{\dagger} \hat{a}_{\alpha, +}), \\ \sqrt{n_{\alpha} - \hat{A}_{\alpha}^{\dagger} \hat{A}_{\alpha}} \hat{A}_{\alpha} &\equiv \frac{1}{2} (\hat{a}_{\alpha, +}^{\dagger} + \hat{a}_{\alpha, -}^{\dagger}) (\hat{a}_{\alpha, +} - \hat{a}_{\alpha, -}), \\ \hat{A}_{\alpha}^{\dagger} \sqrt{n_{\alpha} - \hat{A}_{\alpha}^{\dagger} \hat{A}_{\alpha}} &\equiv \frac{1}{2} (\hat{a}_{\alpha, +}^{\dagger} - \hat{a}_{\alpha, -}^{\dagger}) (\hat{a}_{\alpha, +} + \hat{a}_{\alpha, -}). \end{aligned} \quad (2)$$

The operators  $\hat{A}_{\alpha}$  shift atoms between the two  $\sigma = \pm$  modes of the  $\alpha = \{L, R\}$  dimer. They obey the commutation relation,  $[\hat{A}_{\alpha}, \hat{A}_{\alpha}^{\dagger}] = 1$  and  $[\hat{A}_{\alpha}, \hat{n}_{\alpha}] = 0$ . Consequent application of

the Bogoliubov transformation,  $\hat{A}_{\alpha} = u_{\alpha} \hat{J}_{\alpha} + v_{\alpha} \hat{J}_{\alpha}^{\dagger}$ , transform the single dimer Hamiltonian as

$$\begin{aligned} \hat{H}_{\alpha} &= -\frac{\Omega}{2} (\hat{a}_{+, \alpha}^{\dagger} \hat{a}_{-, \alpha} + H.c.) + \frac{U}{2} \sum_{\sigma} \hat{n}_{\sigma, \alpha} (\hat{n}_{\sigma, \alpha} - 1) \\ &\rightarrow \frac{\Omega}{2} \hat{n}_{\alpha} + \frac{U}{4} \hat{n}_{\alpha} (\hat{n}_{\alpha} - 2) + \sqrt{\Omega(\Omega + U \hat{n}_{\alpha})} \hat{J}_{\alpha}^{\dagger} \hat{J}_{\alpha} \\ &\quad - \frac{U}{8} \frac{4\Omega + U \hat{n}_{\alpha}}{\Omega + U \hat{n}_{\alpha}} \hat{J}_{\alpha}^{\dagger 2} \hat{J}_{\alpha}^2 + \mathcal{O}(U n_{\alpha}^{-1}), \end{aligned} \quad (3)$$

where  $u_{\alpha}$  and  $v_{\alpha}$  are quasihole and particle excitation amplitudes, respectively, and  $\hat{J}_{\alpha}$  obeys the bose commutation relation,  $[\hat{J}_{\alpha}, \hat{J}_{\alpha}^{\dagger}] = 1$ . In deriving Eq. 3, terms that do not commute with  $\hat{J}_{\alpha}^{\dagger} \hat{J}_{\alpha}$  have been neglected. A second HPT applied to the interdimer hopping, reads in the large- $N$  limit,

$$\hat{n}_{L, R} = \frac{1}{2} [N \pm N^{1/2} (\hat{A}^{\dagger} + \hat{A})], \quad (4)$$

where  $\hat{A}$  shifts atoms between the junctions, and obeys the commutation relation,  $[\hat{A}, \hat{A}^{\dagger}] = 1$ . Equation (4) retains total number conservation. Hence, the total Hamiltonian in Eq. (1), including the single dimer Hamiltonians  $\hat{H}_{\alpha}$  and the interdimer coupling, can be written (in units of  $\Omega$ ) as

$$\begin{aligned} \hat{H} &\rightarrow w \hat{A}^{\dagger} \hat{A} + \frac{u}{8} (\hat{A}^{\dagger} + \hat{A})^2 \\ &\quad - \frac{w_{\mathcal{J}}}{2} (\hat{J}_L^{\dagger} \hat{J}_R + \hat{J}_R^{\dagger} \hat{J}_L) - \frac{U_{\mathcal{J}}}{2} \sum_{\alpha=L, R} \hat{J}_{\alpha}^{\dagger 2} \hat{J}_{\alpha}^2 \\ &\quad + \frac{u}{4} \sqrt{\frac{1}{1+u/2}} \frac{(\hat{A} + \hat{A}^{\dagger})}{\sqrt{N}} (\hat{J}_L^{\dagger} \hat{J}_L - \hat{J}_R^{\dagger} \hat{J}_R), \end{aligned} \quad (5)$$

where the effective tunneling frequency and interaction strength of the Josephson excitations are given by

$$w_{\mathcal{J}} = w \frac{1+u/4}{\sqrt{1+u/2}} \quad \text{and} \quad U_{\mathcal{J}} = U \frac{1+u/8}{1+u/2}, \quad (6)$$

respectively. The two first terms on the r.h.s. of Eq. (5) correspond to Josephson oscillations of particles whereas the third and fourth terms are a Josephson Hamiltonian for the excitations with effective attractive interaction between them. The last term couples the two oscillations (due to the dependence of the fast internal dimer frequencies on particle number). In addition to  $N$ , the total number of excitations  $J = \sum_{\alpha=L, R} \hat{J}_{\alpha}^{\dagger} \hat{J}_{\alpha} \rightarrow j_L + j_R$  is also conserved by the approximate Hamiltonian (5). Thus, while the conservation of  $N$  is strict,  $J$  is an adiabatic invariant.

## IV. NUMBER OF EXCITATIONS

The number of excitations in the two subsystems was evaluated in Ref. [49] using a semiclassical approach. Given the energy  $E_{\alpha}$  and the number of particles  $n_{\alpha}$  of the  $\alpha = L, R$  Bose-Josephson subsystem, the number of excitations  $j_{\alpha}$  is just the classical action, i.e., the phase space area enclosed by the classical energy contour in units of the effective Planck constant  $h = 4\pi/n_{\alpha}$ . This area can be analytically evaluated for the elliptical energy contours encountered as long as  $u_{\alpha} \equiv$

TABLE I. Notation of subspace dimensions used throughout the manuscript

Symbol	Dimension
$D$	Hilbert space of the composite system
$D^{(J)}$	$J$ th shell of the composite system's spectrum
$D^{(n_L)}$	$n_L$ th symmetry sector of the composite system
$d_\alpha(n_L)$	Dimension of $\alpha = L, R$ Hilbert space with $n_L$ particles in L
$d_{n_\alpha}$	Rank of the $\hat{\rho}^{(n_\alpha)}$ sector of $\hat{\rho}_\alpha$

$U n_\alpha / \Omega \leq 1$ , resulting in the expression

$$j_\alpha = \frac{1}{2} - \frac{1}{\pi} \text{Re} \left[ 2 \cos \eta_\alpha \frac{K\left(\frac{1 - ie^{-i\eta_\alpha} u_\alpha}{1 + ie^{i\eta_\alpha} u_\alpha}\right)}{\sqrt{1 + ie^{i\eta_\alpha} u_\alpha}} + \frac{2i}{u_\alpha} \sqrt{1 + ie^{i\eta_\alpha} u_\alpha} E\left(\frac{1 - ie^{-i\eta_\alpha} u_\alpha}{1 + ie^{i\eta_\alpha} u_\alpha}\right) + \frac{ie^{i\eta_\alpha} (1 - ie^{-i\eta_\alpha} u_\alpha) \Pi\left(ie^{-i\eta_\alpha} u_\alpha \middle| \frac{2iu_\alpha \cos \eta_\alpha}{1 + ie^{i\eta_\alpha} u_\alpha}\right)}{\sqrt{1 + ie^{i\eta_\alpha} u_\alpha}} \right], \quad (7)$$

where  $K(m)$ ,  $E(m)$ , and  $\Pi(n|m)$  are respectively the complete elliptic integrals of the first, second, and third kinds, and  $\eta_\alpha = \arcsin[2E_\alpha / (\Omega n_\alpha)]$  is used to parametrize  $-\Omega n_\alpha / 2 < E_\alpha < \Omega n_\alpha / 2$  to the  $[-\pi/2, \pi/2]$  range. While the expression of Eq. (7) is admittedly convoluted, it can be verified that in the limit where  $u_\alpha \ll 1$ , it reduces to

$$j_\alpha = \frac{E_\alpha + \Omega n_\alpha / 2}{\sqrt{\Omega(\Omega + U n_\alpha)}} \approx \frac{E_\alpha}{\Omega} + \frac{n_\alpha}{2}, \quad (8)$$

which is just the excitation energy over the one-dimer Josephson frequency, as appropriate for the equally spaced levels in the harmonic Josephson limit.

Below we denote the total particle and excitation numbers as  $N = n_L + n_R$  and  $J = j_L + j_R = 0, 1, \dots, N$ , respectively, and the corresponding particle and excitation imbalances as  $n = n_L - n_R = -N, \dots, N$  and  $j = j_L - j_R = -J, \dots, J$ , respectively.

## V. NOTATION OF SUBSPACE DIMENSIONS

The characterization of the many-body spectrum for the coupled dimers model and the evaluation of bipartite entanglement limits for the resulting eigenstates, require the specification of several subspace dimensions. To improve clarity, the notation of these dimensions is summarized in Table I. The following relations hold:

(i) The Hilbert space dimension for the composite four-mode system:

$$D = \frac{(N+1)(N+2)(N+3)}{6}. \quad (9)$$

(ii) The number of eigenstates in the  $J$ th shell (see below) of the composite's system spectrum:

$$D^{(J)} = (J+1)(N+1-J). \quad (10)$$

The total number of states in all shells is of course the Hilbert space dimension:  $\sum_{J=0}^N D^{(J)} = D$ .

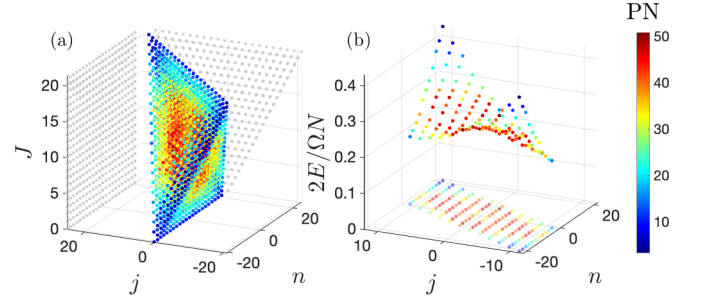


FIG. 1. Spectrum of decoupled dimers. (a) The eigenstates of the double-dimer model with  $N = 21$ ,  $\omega = 0$ , and  $u = 0.5$ , arranged according to the good quantum numbers  $n$ ,  $j$ , and  $J$ . Each eigenstate is colored according to its participation number in the exact eigenbasis with the same parameters except  $\omega = 0.082$ . Grey points mark the projections onto the  $\{n, J\}$  and  $\{j, J\}$  planes; (b) The energies of the  $J = 11$  shell of the spectrum in (a) and its projection onto the  $\{n, j\}$  plane. The  $J = 11$  shell contains  $D^{(11)} = 132$  states.

(iii) Subsystem Hilbert space dimensions when there are  $n_L$  particles in the L subsystem and  $N - n_L$  particles in the R subsystem:

$$d_L(n_L) = n_L + 1, \quad d_R(n_L) = N - n_L + 1. \quad (11)$$

(iv) Dimension of the  $n_L$ th block of the composite's system density matrix:

$$D^{(n_L)} = d_L(n_L) \times d_R(n_L). \quad (12)$$

It is easily verified that  $\sum_{n_L=0}^N D^{(n_L)} = D$ .

(v) Maximum number of non-zero eigenvalues in the  $d_\alpha(n_L)$  dimensional block  $\hat{\rho}_\alpha^{(n_L)}$  of the reduced  $\alpha = L, R$  subsystem density matrices:

$$d_{n_\alpha} = \text{Rank}(\hat{\rho}_\alpha^{(n_L)}) = \min\{d_L(n_L), d_R(n_L)\}. \quad (13)$$

## VI. EIGENSTATES

### A. The unperturbed basis

In the absence of interdimer coupling ( $\omega = 0$ ), the two-dimer energy eigenstates are direct products of single dimer eigenstates in the form

$$|\mu\rangle = |N, J, n, j\rangle = |n_L, j_L\rangle \otimes |n_R, j_R\rangle, \quad (14)$$

with  $N, J, n, j$  being good quantum numbers, as illustrated in Fig. 1(a). The dimension of each fixed- $J$  shell, i.e., the number of states in the  $J$ th layer of the plotted spectrum in Fig. 1(a), is  $D^{(J)}$ . The energies of one such  $J$  shell in the middle of the spectrum are plotted in Fig. 1(b). Within this shell, the energies of high  $|n|$  eigenstates are elevated due to the repulsive interaction between particles. By contrast, the energies of high  $|j|$  eigenstates are lowered due to the effective repulsion between the Josephson excitations in Eq. (5).

### B. Exact spectrum

For finite  $\omega$  we can numerically diagonalize the Hamiltonian in Eq. (1) to obtain the exact eigenstates  $|\nu\rangle$ . Projecting the unperturbed states of Eq. (14) onto the exact basis to obtain  $p_{\nu,\mu} = |\langle \nu | \mu \rangle|^2$ , we can calculate the *participation number*  $\text{PN}_\mu = (\sum_\nu p_{\nu,\mu}^2)^{-1}$ , estimating the number of exact

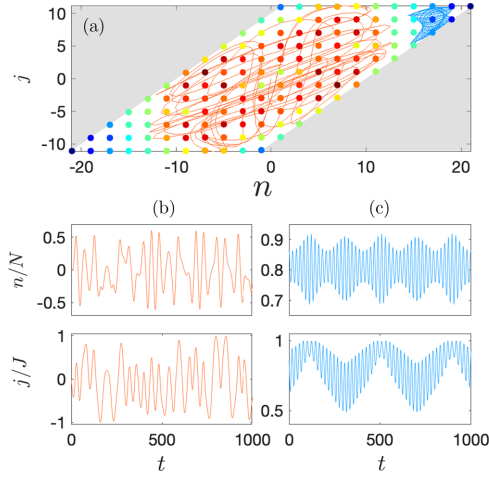


FIG. 2. Mixed structure of the fixed  $J$  shells. (a) The  $J = 11$  shell of the coupling-free spectrum from Fig. 1 overlaid on representative classical trajectories launched at  $J = 11$ ,  $n = j = 0$  (orange) and  $J = 11$ ,  $n = 18.2$ , and  $j = 9.3$  (blue), with the same parameters. The relative interdimer phase of both trajectories is  $\varphi_{LR} = 0$ . The dynamics of the particle and joston imbalances  $n, j$  for the same trajectories is plotted in panels (b) and (c), respectively.

eigenstates that contribute to the unperturbed state  $|\mu\rangle$ . The participation numbers in the  $\omega = 0.082$  basis are denoted by color in Fig. 1. It is clear that the midspectrum fixed  $J$  surfaces contain two pairs of regions with low participation, corresponding to the maxima and minima of the energy surface. These localization regions are separated by a large high-participation ergodic region around the central energy saddle point.

In Fig. 2 the same  $J$  shell of the unperturbed spectrum is plotted over two representative classical trajectories. The participation numbers in the finite-coupling basis correlate well with the classical phase space structure for the same parameters, which due to mutual conservation of  $J$  and  $E$  separates into two pairs of integrable islands in which either particles or excitations are macroscopically self-trapped, and a central chaotic region, explored ergodically by all trajectories launched in it.

For finite interaction,  $n$  and  $j$  are no longer good quantum numbers. Due to its symmetry, the exact eigenstates of the coupled-dimers system belong to one of the four irreducible representations of the dihedral group  $D_2$ . Therefore, the expectation values of the particle and excitation imbalance are  $\langle n \rangle = \langle j \rangle = 0$ . Therefore, in Fig. 3(a) we classify the exact eigenstates according to the standard deviations  $\sigma_n = \sqrt{\langle n^2 \rangle}$  and  $\sigma_j = \sqrt{\langle j^2 \rangle}$ . Each state is colored according to its participation number in the unperturbed basis  $\text{PN}_v = (\sum_{\mu} p_{v,\mu}^2)^{-1}$ . Since the timescale separation between fast intradimer motion and slow interdimer particle and excitation exchange is maintained,  $J$  is conserved so that the exact eigenstates only mix zero-coupling states within a *single*  $J$  shell. This is evident in the layering of the spectrum in shells with integer value of  $(J)$ .

Plotting a fixed  $J = J_0$  shell of the exact spectrum in Fig. 3(b), we identify three representative states for which we plot the probability distribution  $p_{n,j}(v) = |\langle v|N, J_0, n, j \rangle|^2$  (it was verified that  $\sum_{n,j} p_{n,j} = 1$ , i.e., that there is no projection

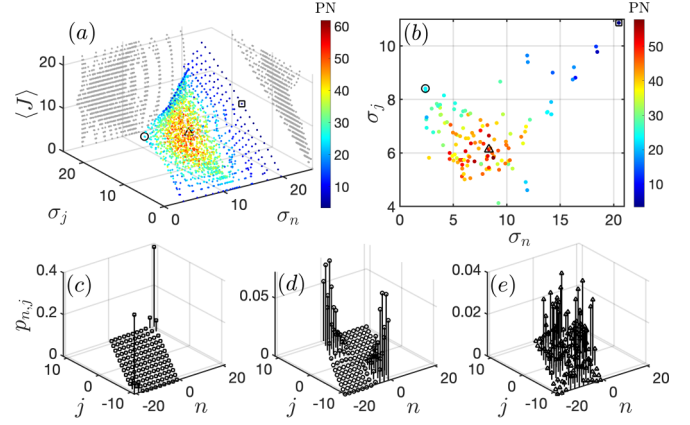


FIG. 3. Coupled dimers spectrum. (a) The eigenstates of the double-dimer model with  $N = 21$ ,  $\omega = 0.082$ , and  $u = 0.5$ , arranged according to their particle-imbalance variance  $\sigma_n = \sqrt{\langle n^2 \rangle}$ , excitation-imbalance variance  $\sigma_j = \sqrt{\langle j^2 \rangle}$ , and mean number of excitations  $\langle J \rangle$ . Each eigenstate is colored according to its participation number in the unperturbed basis set; (b) The  $J = 11$  shell of the spectrum in (a). Markers in (a) and (b) mark the states with the minimum  $\sigma_n$  ( $\circ$ ), the maximum  $\sigma_n$  ( $\square$ ), and the maximum Shannon entropy  $\mathcal{H}$  ( $\triangle$ ) within this  $J$  shell; (c–e) The probability distribution  $p_{n,j}$  for the marked states in (a) and (b) with the same marker convention.

onto states with  $J \neq J_0$ ). The states with high  $\sigma_n$  [Fig. 3(c)] are macroscopic cat states, i.e., superpositions of localized states supported by the integrable particle-self-trapping islands. Similarly, states with high  $\sigma_j$  and low  $\sigma_n$  [Fig. 3(d)] are joston macroscopic catstates, depicting similarly populated dimer subsystems with the excitations in a superposition of all-L and all-R. In between these macroscopic superpositions that come as odd-even doublets with spacing that vanishes exponentially with  $h$  lie the high participation states distributed ergodically over the classically chaotic region of the  $J$  shell [Fig. 3(e)]. The chaoticity of the eigenstates  $|\nu\rangle$  can be quantified by their *Shannon entropy*,

$$\mathcal{H}_\nu = - \sum_{m=1}^D p_{\nu,m} \ln p_{\nu,m} \leq \ln(D) = \mathcal{H}_{\max}, \quad (15)$$

where  $p_{\nu,m} = |\langle m|\nu\rangle|^2$  are the expansion probabilities of  $|\nu\rangle$  in the computational Fock state basis  $|m\rangle = |n_{L,+}, n_{L,-}, n_{R,+}, n_{R,-}\rangle$ . For a fully chaotic system,  $p_{\nu,m}$  may be replaced by independent real random variables from a Gaussian distribution fluctuating around  $1/D$ , resulting in the limiting value [50],

$$\mathcal{H}_{\text{GOE}} = \ln(0.48D). \quad (16)$$

In Fig. 4 the Shannon entropy of the coupled-dimers eigenstates is plotted for three values of the interdimer coupling  $\omega$ , along with the level-spacing statistics obtained by separating the spectrum to the four  $D_2$  symmetry classes and unfolding each class according to the local mean spacing  $\bar{s}(E)$ . Poissonian level statistics  $P(s) = e^{-s}$  indicates integrability, whereas chaos is detected by the Wigner surmise distribution  $P(s) = (\pi/2)se^{-\pi s^2/4}$ . When the coupling is weak [Fig. 4(a)] the chaotic region is small and the dynamics takes place mostly in the integrable self trapping islands, where  $|n|$  is still a good

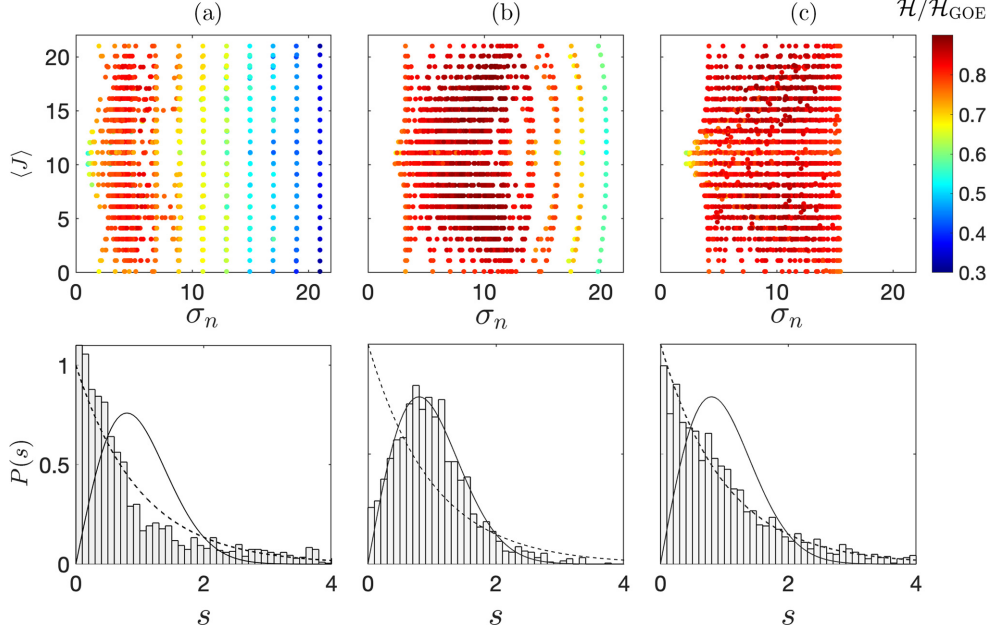


FIG. 4. Level spacing statistics. The coupled-dimers spectrum (top), colorcoded according to the Shannon entropy  $\mathcal{H}$ , and the level spacing statistics (bottom) at  $\omega = 0.01$  (a),  $0.082$  (b), and  $0.5$  (c). Other parameters are the same as in Fig. 3

quantum number. Level spacing statistics is therefore nearly Poissonian. The chaotic sea grows with  $\omega$ , peaking [Fig. 4(b)] at the value used in Fig. 1 and Fig. 3 (the exact parameters for maximizing chaos were determined by analysis of the Brody parameter [51] and the adjacent spacing correlation function [52]). Further increase in  $\omega$  restores integrability because the dynamics becomes linear [Fig. 4(c)]. Note also that when  $\omega$  becomes comparable with the internal dimer frequencies, jostion number conservation is violated due to the breakdown of adiabaticity so that  $\langle J \rangle$  can take noninteger values.

Below, we aim to characterize the number-resolved bipartite entanglement between the Josephson qubits for the coupled-dimers eigenstates, and correlate it with their chaos measure.

## VII. BIPARTITE ENTANGLEMENT

### A. Reduced subsystem density matrices

Consider the bipartition into the L, R dimer subsystems. The state of the system can be expanded in any arbitrary bipartite basis,

$$|\psi\rangle = \sum_{n_L=0}^N \sum_{l=1}^{d_L(n_L)} \sum_{r=1}^{d_R(n_L)} c_{n_L, l, r} |n_L, l\rangle |N - n_L, r\rangle, \quad (17)$$

where  $|n_L, l\rangle$  and  $|N - n_L, r\rangle$  are one-dimer basis states for  $n_L$  and  $n_R = N - n_L$  particles in the L and R dimer, respectively. Given a fixed  $n_L$  sector of the bipartite basis, the Hilbert space dimensions of the two subsystems are  $d_L(n_L) = n_L + 1$  and  $d_R(n_L) = N - n_L + 1$ . For example, one may use the Fock basis  $|n_\alpha, l\rangle = |\ell, m\rangle$  where  $\ell = n_\alpha/2$  and  $m = (n_{+, \alpha} - n_{-, \alpha})/2 = n_\alpha - 2n_{-, \alpha}$  with  $n_{-, \alpha} = 0, 1, \dots, n_\alpha$ . Or, alternatively, the one-dimer energy eigenstates  $|n_\alpha, j_\alpha\rangle$  as in Eq. (14).

Regardless of the choice of subsystem basis, the  $U(1)$  symmetry of the Hamiltonian in Eq. (1) means that the pure density matrix of the composite system  $\hat{\rho} = |\psi\rangle\langle\psi|$  is block diagonal, with the  $n_L$  block having dimension  $D^{(n_L)}$ . Therefore, the reduced density matrix of the L subsystem  $\hat{\rho}_L = \text{Tr}_R \hat{\rho}$  is also block diagonal

$$\hat{\rho}_L = \sum_{n_L=0}^N \hat{\rho}_L^{(n_L)}, \quad (18)$$

with the  $n_L$ th block given as

$$\hat{\rho}_L^{(n_L)} = \sum_{l, l'=1}^{d_L(n_L)} \rho_{l, l'}^{n_L} |n_L, l\rangle\langle n_L, l'|, \quad (19)$$

and its matrix elements are

$$\rho_{l, l'}^{n_L} = \sum_{r=1}^{d_R(n_L)} c_{n_L, l', r}^* c_{n_L, l, r}. \quad (20)$$

The formal dimension of the  $\rho_L^{(n_L)}$  block is  $d_L(n_L)$  but it only has a maximum of  $d_{n_L}$  nonzero eigenvalues. The eigenvalues of the reduced density matrix of the R subsystem  $\hat{\rho}_R = \text{Tr}_L \hat{\rho}$  are the same as those of  $\hat{\rho}_L$ .

### B. Number resolved entanglement

Diagonalizing the reduced one-dimer density matrix and expressing the nonzero eigenvalues as

$$\lambda_i^{(n_L)} = e^{-\xi_i^{(n_L)}}, \quad (21)$$

with  $n_L = 1, \dots, N$  and  $i = 1, \dots, d_{n_L}$ , we obtain the symmetry-resolved *entanglement spectrum*  $\xi_i^{(n_L)}$  [2, 11]. The entanglement spectra of the three representative states in Fig. 3 are shown in Fig. 5. The reduced subsystem

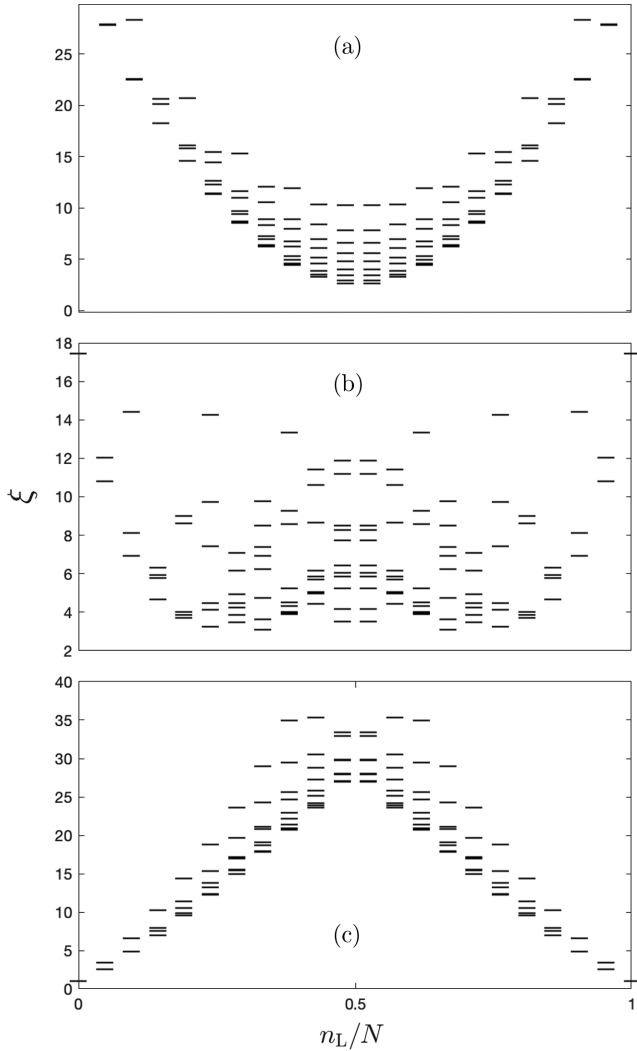


FIG. 5. Entanglement spectra. The number-resolved entanglement spectra of representative states marked by (a)  $\circ$ , (b)  $\triangle$ , and (c)  $\square$  in Fig. 3.

density matrix for the island cat states is dominated by few eigenvalues in the populated integrable regions. In particular, for the “population cat state” in Fig. 3(c), it is clear that the distribution decays exponentially across the chaos border as befitting particle tunneling, whereas for the “excitation cat state” in Fig. 3(d) the  $n$  distribution is Gaussian, as expected for a superposition of coherent states localized in the two  $j$  islands with  $n \approx 0$ . By contrast, for the chaotic states we observe many eigenvalues of comparable magnitude, spread throughout the chaotic sea. The bipartite entanglement entropy of the chaotic states should thus be much larger than that of the island-supported eigenstates.

Given the symmetry resolved entanglement spectrum, the probability for each symmetry sector, i.e., the probability of finding  $n_L$  particles in the L subsystem and  $N - n_L$  particles in the R subsystem is

$$p_{n_L} = \sum_{i=1}^{d_{n_L}} \lambda_i^{(n_L)}. \quad (22)$$

The total entanglement entropy between the two dimer subsystems

$$S = -\text{Tr}(\hat{\rho}_L \ln \hat{\rho}_L) = \sum_{n_L=0}^N S^{(n_L)} \quad (23)$$

can thus be written as the sum of the symmetry-resolved entanglement entropies [41–43]

$$\begin{aligned} S^{(n_L)} &= -\text{Tr}(\hat{\rho}_L^{(n_L)} \ln \hat{\rho}_L^{(n_L)}) \\ &= -\sum_{i=1}^{d_{n_L}} \lambda_i^{(n_L)} \ln \lambda_i^{(n_L)}. \end{aligned} \quad (24)$$

### VIII. ENTANGLEMENT OF ERGODIC STATES

Having defined the number resolved entanglement entropy, we turn to predict its expected form for states corresponding to different semiergodic ensembles. These include uniform canonical states, canonical random states that account for fluctuations about the uniform mean, microcanonical states spread on a single energy shell, and GGE states where ergodicity only applies to a restricted fixed  $J$  region within the energy shell.

#### A. Uniform states

Consider a completely uniform state  $|\psi_{\text{erg}}\rangle$  defined by Eq. (17) with  $|c_{n_L, l, r}| = 1/\sqrt{D}$  for all  $n_L, l, r$ . The population distribution for such a state is proportional to the density of states

$$p_{n_L}^{\text{erg}} = \frac{D^{(n_L)}}{D}. \quad (25)$$

Each  $\hat{\rho}_L^{(n_L)}$  block of the reduced one-dimer density matrix will have  $d_{n_L}$  equal eigenvalues  $\lambda_i^{(n_L)} = p_{n_L}^{\text{erg}}/d_{n_L}$ , hence the number resolved entropy is

$$S_{\text{erg}}^{(n_L)} = -p_{n_L}^{\text{erg}} \ln \frac{p_{n_L}^{\text{erg}}}{d_{n_L}}, \quad (26)$$

and the total bipartite entanglement entropy is

$$S_{\text{erg}} = \sum_{n_L=0}^N S_{\text{erg}}^{(n_L)} < \ln \left( \sum_{n_L=0}^N d_{n_L} \right) = S_{\text{max}}. \quad (27)$$

#### B. Canonical random states

To account for fluctuations over the ergodic mean, consider a random canonical state  $|\psi_{\text{GOE}}\rangle$  in which

$$c_{n_L, l, r} = \frac{z_{n_L, l, r}}{\sqrt{D}}, \quad (28)$$

where  $z_{n_L, l, r}$  are real random numbers, picked from a normal distribution with zero mean and unit variance. Such states emulate the eigenstates of random matrices from a Gaussian Orthogonal Ensemble (GOE), expected for fully chaotic systems that are not restricted to one energy shell (e.g., the kicked rotor). While they are not strictly normalized, the mean of their norm is one and the norm fluctuations rapidly decline with  $N$ . Thus, we simply renormalize the state vector by the norm  $\mathcal{N} \approx 1$ . The mean population distribution remains  $p_{n_L}^{\text{erg}}$

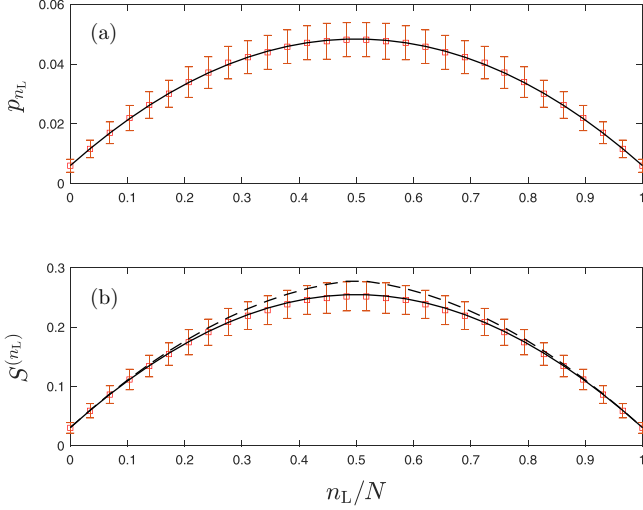


FIG. 6. Entanglement of canonical random states. The particle distribution probability  $p_{n_L}$  and the number-resolved entanglement entropy  $S^{(n_L)}$  are plotted as a function of  $n_L$  in panels (a) and (b), respectively. Symbols and error bars correspond to the mean and standard deviation over an ensemble of  $10^3$  symmetrized canonical random states with  $N = 29$  particles. The solid line in (a) corresponds to the anticipated ergodic distribution  $p_{n_L}^{\text{erg}}$  of Eq. (25), whereas the dashed and solid lines in panel (b) correspond to the estimates of  $S_{\text{erg}}^{(n_L)}$  in Eq. (26) and  $S_{\text{GOE}}^{(n_L)}$  in Eq. (29), respectively.

but the expected entanglement entropies  $S^{(n_L)}$  now include a finite-size fluctuation correction [23,34]

$$\begin{aligned} S_{\text{GOE}}^{(n_L)} &= S_{\text{erg}}^{(n_L)} - \frac{p_{n_L}^{\text{erg}}}{2} \frac{d_{n_L}^2}{D^{(n_L)}} \\ &= S_{\text{erg}}^{(n_L)} - \frac{p_{n_L}^{\text{erg}}}{2} \frac{\min\{d_L(n_L), d_R(n_L)\}}{\max\{d_L(n_L), d_R(n_L)\}} \end{aligned} \quad (29)$$

so that the total entanglement entropy is

$$S_{\text{GOE}} = S_{\text{erg}} - \frac{1}{2} \sum_{n_L=0}^N p_{n_L}^{\text{erg}} \frac{d_{n_L}^2}{D^{(n_L)}}. \quad (30)$$

In Fig. 6 we validate the predictions of Eq. (25) and Eq. (29) by comparison to the mean population distribution and the mean number-resolved entanglement entropy of a numerically generated ensemble of canonical random states. Each random state realization is symmetrized to the  $A_1$  irreducible representation of the  $D_2$  group, and the mean number distribution and entanglement entropy over all realizations are calculated within each  $n_L$  sector. The ergodic number distribution and the finite-size fluctuation correction to the entanglement entropy clearly capture the behavior of the canonical random states.

### C. GGE states

Due to the conservation of  $E$  and  $J$ , the ergodicity of the chaos supported eigenstates is incomplete in the sense that they are restricted to the fixed  $J$  region within the energy shell. The expected population distribution for such states will thus

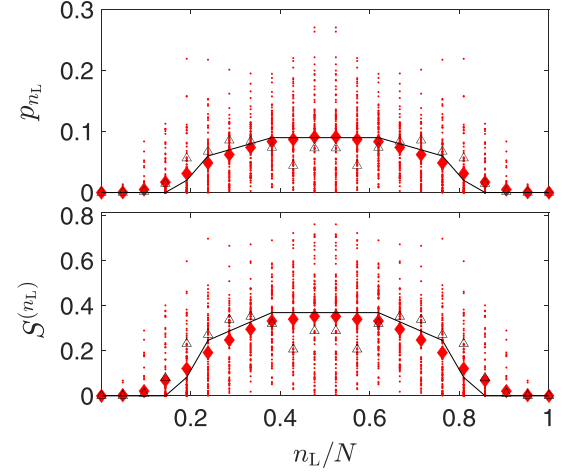


FIG. 7. Entanglement of chaos-supported states. Particle distribution probability (a) and number-resolved entanglement entropy (b) for the  $D_{\text{ch}}^{(J)} = 100$  highest  $\mathcal{H}$  states in the  $J = 11$  shell of the exact spectrum. Diamond symbols mark the mean value, whereas solid lines correspond to the predicted generalized Gibbs ensemble values  $p_{J,n_L}^{\text{GGE}}$  and  $S_{\text{GGE}}^{(J,n_L)}$ . Triangles mark the number resolved entanglement entropy of the chaotic state of Fig. 3. Parameters are the same as in Fig. 3.

differ from  $p_{n_L}^{\text{GOE}}$  and correspond to that of a GGE,

$$p_{J,n_L}^{\text{GGE}} = \frac{D_{\text{ch}}^{(J,n_L)}}{D_{\text{ch}}^{(J)}}, \quad (31)$$

where  $D_{\text{ch}}^{(J)}$  is the total number of unperturbed eigenstates *in the chaotic region* of the  $J$  shell, and  $D_{\text{ch}}^{(J,n_L)}$  is the dimension of the fixed  $n_L$  subset, hence  $\sum_{n_L} D_{\text{ch}}^{(J,n_L)} = D_{\text{ch}}^{(J)}$ .

The expected number-resolved entanglement entropy for the chaos-supported eigenstates in the coupled-dimers system is, accordingly,

$$S_{\text{GGE}}^{(J,n_L)} = p_{J,n_L}^{\text{GGE}} \left( \ln D_{\text{ch}}^{(J)} - \frac{1}{2} \right), \quad (32)$$

so that the total bipartite entanglement entropy  $S_{\text{GGE}}^{(J)} = \ln D_{\text{ch}}^{(J)} - \frac{1}{2}$  depends on the area of the  $J$  shell, rather than on the system's volume. The first term corresponds to the entropy of a uniform state with  $p_{J,n_L} = 1/D_{\text{ch}}^{(J)}$ , whereas the subtracted factor accounts for maximal fluctuations around this mean value.

In Fig. 7, the expressions for the GGE population-distribution in Eq. (31) and entanglement entropy in Eq. (32) are validated by comparison with the corresponding mean values over all the chaotic states in a representative fixed- $J$  shell. While there is an overall good agreement, the entanglement entropy of the chaos supported states is slightly lower than the GGE prediction, indicating larger fluctuations due to the incomplete ergodicity of the eigenstates.

The total bipartite entanglement entropy  $S$  of all the eigenstates of the coupled dimers system is correlated in Fig. 8 with their ergodicity, quantified by the Shannon entropy  $\mathcal{H}$ . The anticipated  $S_{\text{GOE}}$  and  $S_{\text{GGE}}$  estimates match the numerical results for canonical random states and chaos-supported eigenstates, respectively. It is also verified that the chaos-supported states are not entirely ergodic, as their Shannon entropy is somewhat

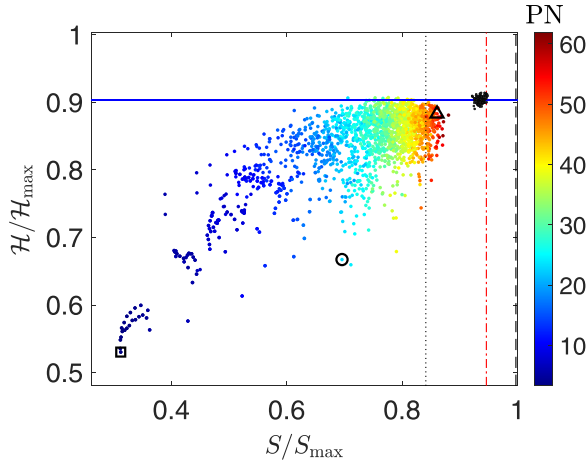


FIG. 8. Correlation between chaos and bipartite entanglement. The Shannon entropy vs the bipartite entanglement entropy of the double dimer eigenstates with  $N = 21$ . Symbols point to the marked representative states in Fig. 3. Black dots correspond to numerically generated canonical random states. The horizontal solid line marks  $\mathcal{H}_{\text{GOE}}$ , whereas the vertical lines mark  $S_{\text{erg}}$  (dashed),  $S_{\text{GOE}}$  (dash-dotted), and  $S_{\text{GGE}} \equiv \max_J(S_{\text{GGE}}^{(J)})$  (dotted).

below  $\mathcal{H}_{\text{GOE}}$ . In comparison, the bipartite entanglement entropy of the island-supported states matches the expectation for macroscopic cat states, for which the reduced density matrix contains only a few (minimally two) nonvanishing eigenvalues.

### IX. EXPERIMENTAL REALIZATION

The experimental relevance of the symmetry-resolved entanglement entropy has been demonstrated in [53–55]. In particular, Ref. [53] outlines a method for measuring  $p_{n_L}$  and  $S^{(n_L)}$  in Bose-Hubbard systems. Projection into the Fock basis  $|m\rangle$  is obtained by a sudden increase of the lattice depth and number-sensitive imaging with single-site resolution. Atom number counting on individual lattice sites in different runs of the experiment then probes the probability distribution  $p_{n_L}$ , and consequently provides the “number participation”  $\text{PN}_n = (\sum_{n_L} p_{n_L}^2)^{-1}$  and the “number entropy”  $S_n = -\sum_{n_L} p_{n_L} \ln p_{n_L}$  that quantify the effective number of contributing  $\hat{\rho}_L^{(n_L)}$  blocks and the interblock entanglement, re-

spectively. The symmetry resolved entanglement  $S^{(n_L)}$ , called the “configurational entropy” in [53], is cleverly probed by monitoring number resolved correlators that quantify the intrablock entanglement via the deviation from separability between the constituent subsystems. One caveat is that the parameter range for linear dependence between these configurational correlators and the symmetry resolved entanglement entropies, is limited. However, systematic studies of the relation between entanglement entropy and subsystem correlations may overcome this problem. The quantities presented in this paper are thus measurable with current experimental techniques.

### X. CONCLUSIONS

The bipartite entanglement of eigenstates of partitioned systems and its relation to chaotic ergodicity are the subject of a growing body of work [23–40]. Most effort has so far been concentrated on fermionic systems and spinchains for which the classical limit is sometimes obscure. The mean-field limit of many-boson systems allows for a relatively simple analysis of the classical phase space structure, and a tractable connection to the resulting eigenstate entanglement entropy and its deviations from complete ergodicity.

The coupled Bose-Josephson system provides an excellent testbed for studying bipartite entanglement in a mixed phase space with partial ergodicity. We have characterized the global phase space structure of this system and correlated it with the structure of the U(1) symmetry-resolved entanglement of midsystem eigenstates supported by the different dynamical regions. The dependence of symmetry-resolved entanglement entropy of random states on the relative size of the constituent subsystems was found to follow the Page formula [23]. The overall entanglement was found to be restricted by incomplete ergodicity due to the adiabatic invariance of the sum of subsystem actions. Future work will establish how bipartite entanglement is affected by the breakdown of jason conservation at strong interdimer coupling and strong interaction.

### ACKNOWLEDGMENT

This research was supported by the Israel Science Foundation (Grant No. 283/18). Valuable discussions with Doron Cohen are greatly appreciated.

- [1] L. Amico, R. Fazio, A. Osterloh, and V. Vedral, Entanglement in many-body systems, *Rev. Mod. Phys.* **80**, 517 (2008).
- [2] N. Laflorencie, Quantum entanglement in condensed matter systems, *Phys. Rep.* **646**, 1 (2016).
- [3] D. Deutsch, Quantum Theory, the Church-Turing principle and the universal quantum computer, *Proc. R. Soc. A (London)* **400**, 97 (1985).
- [4] M. B. Plenio and V. Vedral, Teleportation, entanglement and thermodynamics in the quantum world, *Contemp. Phys.* **39**, 431 (1998).
- [5] S. R. White, Density Matrix Formulation for Quantum Renormalization Groups, *Phys. Rev. Lett.* **69**, 2863 (1992).

- [6] U. Schollwöck, The density-matrix renormalization group, *Rev. Mod. Phys.* **77**, 259 (2005).
- [7] U. Schollwöck, The density-matrix renormalization group in the age of matrix product states, *Ann. Phys.* **326**, 96 (2011).
- [8] A. Osterloh, L. Amico, G. Falci, and R. Fazio, Scaling of entanglement close to a quantum phase transition, *Nature (London)* **416**, 608 (2002).
- [9] T. J. Osborne and M. A. Nielsen, Entanglement in a simple quantum phase transition, *Phys. Rev. A* **66**, 032110 (2002).
- [10] S.-J. Gu, S.-S. Deng, Y.-Q. Li, and H.-Q. Lin, Entanglement and Quantum Phase Transition in the Extended Hubbard Model, *Phys. Rev. Lett.* **93**, 086402 (2004).



- [11] H. Li and F. D. M. Haldane, Entanglement Spectrum as a Generalization of Entanglement Entropy: Identification of Topological Order in Non-Abelian Fractional Quantum Hall Effect States, *Phys. Rev. Lett.* **101**, 010504 (2008).
- [12] P. Calabrese and J. Cardy, Evolution of entanglement entropy in one-dimensional systems, *J. Stat. Mech.* (2005) P04010.
- [13] V. Eisler and I. Peschel, Evolution of entanglement after a local quench, *J. Stat. Mech.* (2007) P06005.
- [14] P. Calabrese and J. Cardy, Entanglement and correlation functions following a local quench: A conformal field theory approach, *J. Stat. Mech.* (2007) P10004.
- [15] L. F. Santos, A. Polkovnikov, and M. Rigol, Entropy of Isolated Quantum Systems after a Quench, *Phys. Rev. Lett.* **107**, 040601 (2011).
- [16] I. Tikhonov, A. Vardi, J. R. Anglin, and D. Cohen, Minimal Fokker-Planck Theory for the Thermalization of Mesoscopic Subsystems, *Phys. Rev. Lett.* **110**, 050401 (2013).
- [17] C. Khripkov, A. Vardi, and D. Cohen, Quantum thermalization: Anomalous slow relaxation due to percolation-like dynamics, *New J. Phys.* **17**, 023071 (2015).
- [18] A. M. Kaufman, M. E. Tai, A. Lukin, M. Rispoli, R. Schittko, P. M. Preiss, and M. Greiner, Quantum thermalization through entanglement in an isolated many-body system, *Science* **353**, 794 (2016).
- [19] C. Khripkov, A. Vardi, and D. Cohen, Many-body dynamical localization and thermalization, *Phys. Rev. A* **101**, 043603 (2020).
- [20] M. Brenes, S. Pappalardi, J. Goold, and A. Silva, Multipartite Entanglement Structure in the Eigenstate Thermalization Hypothesis, *Phys. Rev. Lett.* **124**, 040605 (2020).
- [21] J. A. Kjäll, J. H. Bardarson, and F. Pollmann, Many-Body Localization in a Disordered Quantum Ising Chain, *Phys. Rev. Lett.* **113**, 107204 (2014).
- [22] Y. Huang and J. E. Moore, Excited-state entanglement and thermal mutual information in random spin chains, *Phys. Rev. B* **90**, 220202 (2014).
- [23] D. N. Page, Average Entropy of a Subsystem, *Phys. Rev. Lett.* **71**, 1291 (1993).
- [24] J. M. Deutch, Thermodynamic entropy of a many-body energy eigenstate, *New J. Phys.* **12**, 075021 (2010).
- [25] J. M. Deutsch, Haibin Li, and Auditya Sharma, Microscopic origin of thermodynamic entropy in isolated systems, *Phys. Rev. E* **87**, 042135 (2013).
- [26] L. F. Santos, A. Polkovnikov, and M. Rigol, Weak and strong typicality in quantum systems, *Phys. Rev. E* **86**, 010102 (2012).
- [27] A. Hama, S. Santra, and P. Zanardi, Quantum Entanglement in Random Physical States, *Phys. Rev. Lett.* **109**, 040502 (2012).
- [28] J. Mölter, T. Barthel, U. Schollwök, and V. Alba, Bound states and entanglement in the excited states of quantum spin chains *J. Stat. Mech.* (2014) P10029.
- [29] F. Ares, J. G. Esteve, F. Falceto, and E. Sánchez-Burillo, Excited state entanglement in homogeneous fermionic chains, *J. Phys. A: Math. Theor.* **47**, 245301 (2014).
- [30] M. Storms and R. E. P. Singh, Entanglement in ground and excited states of gapped free-fermion systems and their relationship with Fermi surface and thermodynamic equilibrium properties, *Phys. Rev. E* **89**, 012125 (2014).
- [31] M. Žnidarič, Entanglement of random vectors, *J. Phys. A: Math. Theor.* **40**, F105 (2007).
- [32] V. Alba, Eigenstate thermalization hypothesis and integrability in quantum spin chains, *Phys. Rev. B* **91**, 155123 (2015).
- [33] W. Beugeling, A. Andreanov, and M. Haque, Global characteristics of all eigenstates of local many-body Hamiltonians: participation ratio and entanglement entropy, *J. Stat. Mech.* (2015) P02002.
- [34] L. Vidmar and M. Rigol, Entanglement Entropy of Eigenstates of Quantum Chaotic Hamiltonians, *Phys. Rev. Lett.* **119**, 220603 (2017).
- [35] J. R. Garrison and T. Grover, Does a Single Eigenstate Encode the Full Hamiltonian? *Phys. Rev. X* **8**, 021026 (2018).
- [36] C. Murthy and M. Srednicki, Structure of chaotic eigenstates and their entanglement entropy, *Phys. Rev. E* **100**, 022131 (2019).
- [37] Y. Huang, Universal eigenstate entanglement of chaotic local Hamiltonians, *Nucl. Phys. B* **938**, 594 (2019).
- [38] P. Łydzba, M. Rigol, and L. Vidmar, Eigenstate Entanglement Entropy in Random Quadratic Hamiltonians, *Phys. Rev. Lett.* **125**, 180604 (2020).
- [39] P. Łydzba, M. Rigol, and L. Vidmar, Entanglement in many-body eigenstates of quantum-chaotic quadratic Hamiltonians, *Phys. Rev. B* **103**, 104206 (2021).
- [40] M. Haque, P. A. McClarty, and I. M. Khaymovich, Entanglement of midspectrum eigenstates of chaotic many-body systems: Reasons for deviation from random ensembles, *Phys. Rev. E* **105**, 014109 (2022).
- [41] N. Laflorencie and S. Rachel, Spin-resolved entanglement spectroscopy of critical spin chains and Luttinger liquids, *J. Stat. Mech.* (2014) P11013.
- [42] M. Goldstein and E. Sela, Symmetry-Resolved Entanglement in Many-Body Systems, *Phys. Rev. Lett.* **120**, 200602 (2018).
- [43] J. C. Xavier, F. C. Alcaraz, and G. Sierra, Equipartition of the entanglement entropy, *Phys. Rev. B* **98**, 041106 (2018).
- [44] J. E. Avron and O. Zeitun, Entanglement and the geometry of two qubits *Ann. Phys.* **324**, 470 (2009).
- [45] M. P. Strzys and J. R. Anglin, Four-mode Bose-Hubbard model with two greatly differing tunneling rates as a model for the Josephson oscillation of heat, *Phys. Rev. A* **81**, 043616 (2010).
- [46] M. P. Strzys and J. R. Anglin, Extension of Bogoliubov theory for a many-body system with a time-scale hierarchy: The quantum mechanics of second Josephson oscillations, *Phys. Rev. A* **85**, 053610 (2012).
- [47] C. Khripkov, C. Piermarocchi, and A. Vardi, Dynamics of microcavity exciton polaritons in a Josephson double dimer, *Phys. Rev. B* **88**, 235305 (2013).
- [48] C. Khripkov and A. Vardi, Coherence oscillations between weakly coupled Bose-Hubbard dimers, *Phys. Rev. A* **89**, 053629 (2014).
- [49] S. Ray, J. R. Anglin, and A. Vardi, Prethermalization with negative specific heat, *Phys. Rev. E* **102**, 052107 (2020).
- [50] F. Borgonovi, F. M. Izrailev, L. F. Santos, and V. G. Zelevinsky, Quantum chaos and thermalization in isolated systems of interacting particles, *Phys. Rep.* **626**, 1 (2016).
- [51] T. A. Brody, A statistical measure for the repulsion of energy levels, *Lett. Nuovo Cimento* **7**, 482 (1973).
- [52] Y. Y. Atas, E. Bogomolny, O. Giraud and G. Roux, Distribution of the Ratio of Consecutive Level Spacings in

- Random Matrix Ensembles, *Phys. Rev. Lett.* **110**, 084101 (2013).
- [53] A. Lukin, M. Rispoli, R. Schittko, M. E. Tai, A. M. Kaufman, S. Choi, V. Khemani, J. Léonard, and M. Greiner, Probing entanglement in a many-body-localized system, *Science* **364**, 256 (2019).
- [54] D. Azses, R. Haenel, Y. Naveh, R. Raussendorf, E. Sela and E. G. Dalla Torre, Identification of Symmetry-Protected Topological States on Noisy Quantum Computers, *Phys. Rev. Lett.* **125**, 120502 (2020).
- [55] V. Vitale, A. Elben, R. Kueng, A. Neven, J. Carrasco, B. Kraus, P. Zoller, P. Calabrese, B. Vermersch, M. Dalmonte, Symmetry-resolved dynamical purification in synthetic quantum matter, *SciPost Phys.* **12**, 106 (2022).